Redirection of sound in straight fluid channel with elastic boundaries

Andrey Bozhko,[1] Victor M. García-Chocano,[2] José Sánchez-Dehesa,[2] and Arkadii Krokhin[1,*]
[1]*Department of Physics, University of North Texas, P.O. Box 311427, Denton, Texas 76203, USA*
[2]*Universidad Politécnica de Valéncia, Camino de Vera s/n, E-46022 Valencia, Spain*
(Received 30 July 2014; revised manuscript received 23 February 2015; published 16 March 2015)

A fluid channel clad between two solid plates is an acoustic waveguide where excitation of elastic waves at the channel boundaries has been usually neglected. This work develops a rigorous theory of scattering of sound by a finite-length fluid channel which takes into account excitation of elastic eigenmodes of two plates acoustically coupled through a fluid channel. The theory predicts an evidently contradictory result that the transmission and reflection coefficients of a nondissipative channel do not sum up to one. Moreover, they both exhibit deep minima at the same series of frequencies. It is shown that conservation of acoustic energy occurs due to redirection of sound, since part of the acoustic flux escapes into the solid plates. This scattering becomes possible because the uniform flatness of the boundaries of a straight channel is broken by vibrations. Theoretical predictions are supported by the experiments with ultrasound transmission through a narrow slit obtained between two brass or aluminum plates submerged in water. Measured transmission spectra exhibit deep minima exactly at the frequencies where the theory predicts strong redirection of sound.

DOI: 10.1103/PhysRevB.91.094303 PACS number(s): 43.20.+g, 43.30.+m, 46.40.−f, 42.25.Fx

I. INTRODUCTION

The existence of elastic waves confined to the superficial region of an infinite homogeneous solid, first predicted by Lord Rayleigh [1], plays an important role in various fields like geophysics, acoustoelectronics, and seismology. It is shown here that elastic surface waves also have paramount importance in transmission of ultrasound through narrow fluid channels formed by two elastic media. Intensive study of sound transmission through narrow apertures has shown that this phenomenon is much richer than it was predicted by the classical theory of diffraction at zero-width ideal rigid screens [2,3]. Transmission through an aperture in a finite-thickness rigid wall can differ essentially [4,5]. Fabry-Pérot resonances which exist for a subwavelength slit of width d in a solid screen with finite thickness give rise to unexpected increase of the transmission with the resonant wavelength, $T \sim \lambda_n/d$ [6]. A periodic set of subwavelength slits or holes in a rigid screen may transmit almost 100% of incoming sound at the resonant frequencies [7]—a phenomenon akin to extraordinary optical transmission [8]. For both types of waves the extraordinary transmission is due to coupling between the Fabry-Pérot cavity mode with two surface waves excited on both faces of the screen. Acoustic surface wave may be excited at the interface between a fluid and a rigid screen if the faces of the screen are periodically corrugated [9]. If the apertures are arranged periodically along the surface, they themselves serve as corrugations [6,10]. If there is a single aperture in a screen (a slit) then the faces of the screen are additionally corrugated. In the latter case the transmission through this slit exhibits a sharp resonant peak and also very effective collimation of sound [11,12]. It is interesting that periodically perforated thick slab may exhibit ideal reflection, apart from extraordinary transmission, as it was earlier predicted in Ref. [13].

Recent calculations of the transmissivity through a finite-thickness aperture are based on expansion of pressure over waveguide modes. The modes are the solutions of the wave equation with rigid-body boundary conditions. This method was proposed in Ref. [11] for acoustic transmission and in Refs. [14–16] for transmission of electromagnetic waves. The rigid-body approximation is usually justified by high contrast between the impedances of the fluid and the screen. However, the acoustic coupling between them is strongly enhanced near the frequency of the Fabry-Pérot resonance, i.e., when a quasistanding wave is formed inside a fluid channel. Due to the resonance, even weak coupling may be sufficient for effective exchange of energy between the fluid and elastic screens. Synchronized oscillations of the fluid and the screens are accompanied by deformation of the elastic boundaries of the channel. While this surface deformation looks similar to propagating Rayleigh wave [17], there are essential differences. First, the dispersion equation is nonlinear, unlike the one for the Rayleigh waves. Second, there is a nonzero flux of acoustic energy from fluid to metal, which does not exist for evanescent (inside metal) Rayleigh waves. Due to this flux a finite-length fluid channel serves as a redirecting acoustic antenna. Collective vibrations of the screens coupled through the fluid and driven by external wave can be represented as a superposition of the eigenmodes of the whole system. Deep minima in transmission occur when two eigenmodes propagating in opposite directions interfere destructively, forming a quasistanding wave. Deep minima have been reported in Ref. [18] and their unusual nature has remained unclear. Here we develop a theory of sound transmission through a slit formed by two elastic solid plates. We solve the eigenvalue problem for the whole system which consists of two elastic infinite plates coupled through a straight fluid channel. The acoustic field is expanded over the set of eigenfunctions which describe synchronized vibrations of the whole system. Each eigenfunction is characterized by complex eigenvector, i.e., these eigenfunctions are *inhomogeneous* plane waves. They form a nonorthogonal basis, like the well-known Rayleigh-Lamb modes describing vibrations of an isolated solid elastic plate [19]. Lack of orthogonality presents certain mathematical difficulties in calculations. Nevertheless, the expansion over this nonorthogonal basis converges

*arkady@unt.edu

sufficiently fast, providing very good agreement with experimental results in the whole frequency range. Using the proposed theory we show that at the frequencies when the deep minima in transmission are observed the reflection is also minimal. This occurs due to formation of quasistanding Rayleigh wave in the whole system. Since the transmission and reflection are strongly suppressed, the only way for the accumulated elastic energy to escape is radiation into metal. This means that the eigenfunctions are leaky modes, similar to quasisurface waves at solid-fluid interfaces studied in Refs. [17,20,21]. It was also demonstrated that leaky (or quasiguided) elastic modes give a resonant contribution to sound transmission through a glass plate decorated by periodically arranged polymer spheres [22].

The rate of radiation into metal is relatively high, i.e., a straight fluid channel serves as redirecting acoustic antenna. The proposed mechanism is very different from the strong suppression of sound transmission through a periodic arrangement of holes in a rigid screen [13,23,24]. The latter is due to destructive interference between the Fabry-Pérot cavity mode and the Fourier component of the acoustic field in the fluid with the wavelength equal to the period of perforation. This Fano-like resonance exists even in the rigid-body approximation and is manifested as total reflection of sound wave from the perforated solid plate. Unlike this, the proposed effect of redirection of sound leads to suppression of both, transmission and reflection, and it vanishes in the rigid-body approximation.

II. SCATTERING PROBLEM FOR SOUND WAVE IMPINGING AT ELASTIC SCREEN WITH STRAIGHT FLUID CHANNEL

In the experiment a sound wave was generated and detected by two 1.5 in. transducers immersed in a water tank at equal distance $l = 8$ cm from the plates. A slit between two square brass or aluminum plates with side $L = 12$ cm is located in front of the transducers. A sound wave was incident normally to the slit and the transmission spectrum was measured with compensation of the nonflat frequency response of the piezoelectric transducers. The plate thickness h defines the length of the water channel and its width d (the slit's aperture) is maintained by means of a sample holder that fixes both metal plates. This experimental setup is schematically shown in the inset to Fig. 1.

To calculate the transmission of a plane sound wave coming from the left, $(p_0/i\omega\rho_f)\exp(ik_0x - i\omega t)$, we introduce the potentials of the reflected $R(x,z)$ $(x < 0)$ and transmitted $T(x,z)$ $(x > h)$ acoustic fields. They define velocity and pressure in the fluid (e.g., $\mathbf{v} = \nabla R$, $p = p_0 + i\omega\rho_f R$ for $x < 0$). Here $k_0 = \omega/c_f$, ρ_f is the density, and c_f is the speed of sound in the fluid. The potentials of the reflected and transmitted fields are represented through their Fourier integrals

$$R(x,z) = \int_{-\infty}^{+\infty} r(k)e^{ikz - i\beta(k)x}dk, \quad x \leqslant 0, \tag{1}$$

$$T(x,z) = \int_{-\infty}^{+\infty} t(k)e^{ikz + i\beta(k)(x-h)}dk, \quad x \geqslant h. \tag{2}$$

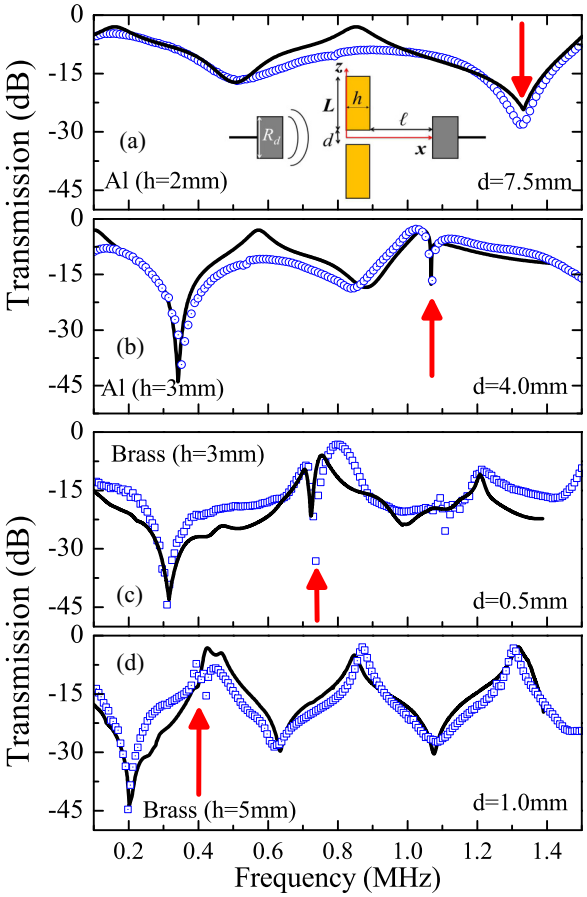

FIG. 1. (Color online) Sound transmission spectra of a water slit between two aluminum (a),(b) and brass (c),(d) plates. Experimental results are shown by circles for aluminum and by squares for brass. Calculated spectra are shown by solid lines. The minima corresponding to excitation of the slow mode are marked by vertical arrows. Inset: experimental setup showing the geometrical parameters of the slit.

Here the longitudinal (along x) component of the wave vector is defined as $\beta(k) = \sqrt{k_0^2 - k^2}$ for $|k| < k_0$ and $\beta(k) = i\sqrt{k^2 - k_0^2}$ for $|k| > k_0$.

In the region $0 \leqslant x \leqslant h$ occupied by the fluid channel and the elastic plates the potentials can be expanded over a set of eigenfunctions of the corresponding infinite channel

$$B(x,z) = \sum_n (b_n^+ e^{i\beta_n x} + b_n^- e^{-i\beta_n x})\cos k_n z, \tag{3a}$$

$$L(x,z) = \sum_n (l_n^+ e^{i\beta_n x} + l_n^- e^{-i\beta_n x})e^{-\nu_n|z|}, \tag{3b}$$

$$S(x,z) = \sum_n (s_n^+ e^{i\beta_n x} - s_n^- e^{-i\beta_n x})e^{-\eta_n|z|}, \tag{3c}$$

where B is the velocity potential of the fluid $[\mathbf{v}(x,z) = \nabla B, |z| \leqslant d/2]$ and the potentials L and S give the displacement vector in the plates,

$$\mathbf{u} = \nabla L + \nabla \times (S\hat{\mathbf{y}}), \quad |z| \geqslant d/2. \tag{4}$$

The transversal parts of the wave vectors in the fluid and in the plates are defined as

$$k_n = \sqrt{k_0^2 - \beta_n^2}, \quad \nu_n = \sqrt{\beta_n^2 - k_l^2}, \quad \eta_n = \sqrt{\beta_n^2 - k_t^2},$$
$$\mathrm{Re}(\nu_n, \eta_n) > 0, \quad k_l = \omega/c_l, \quad k_t = \omega/c_t. \tag{5}$$

c_t (c_l) is the speed of transversal (longitudinal) sound in the plates. Our final goal is calculation of the reflected and transmitted acoustic fields in the fluid. Transmitted $t(k)$ and reflected $r(k)$ amplitudes in Eqs. (1) and (2) are related to the coefficients b_n, l_n, and s_n in the linear expansions (3). These linear relations can be obtained through the boundary conditions at the vertical ($x = 0, h$) and horizontal ($z = \pm d/2$) surfaces of the structure.

III. DISPERSION OF EIGENMODES IN INFINITE CHANNEL

The eigenmodes in Eq. (3) are labeled by integer n which numerates the roots of the dispersion equation $\beta_n = \beta_n(\omega)$. This equation is derived in Appendix A from the continuity of force and velocity at the boundaries $z = \pm d/2$ [18,25]. Since the system is symmetric with respect to the plane $z = 0$ the eigenmodes are either even or odd functions of z. Odd modes are excited at oblique incidence or if the plates are made of different metals [26]. In our case only even modes can be excited. The dispersion equation for these modes is written as follows:

$$(2-\xi^2)^2 - 4\sqrt{1-\xi^2}\sqrt{1-\frac{c_t^2}{c_l^2}\xi^2} = \pm\frac{\rho_f}{\rho_m}\xi^4\sqrt{\frac{1-(c_t/c_l)^2\xi^2}{(c_t/c_f)^2\xi^2-1}}\cot\left(\frac{\omega}{\xi}\frac{d}{2c_t}\sqrt{\frac{c_t^2}{c_f^2}\xi^2-1}\right). \tag{6}$$

Here ρ_m is the density of the elastic plates. Each root ξ_n of the dispersion equation gives the normalized phase velocity $\xi_n = \omega/c_t\beta_n$ of the coupled quasisurface waves. Since the coupling between these waves occurs through the fluid, the right-hand side (RHS) of Eq. (6) is proportional to the ratio ρ_f/ρ_m. When $\rho_f/\rho_m = 0$ the vibrations of the plates are uncoupled and Eq. (6) is reduced to the well-known cubic equation with respect to ξ^2. Its unique solution $\xi = \xi_R$ defines the velocity of dispersionless surface Rayleigh wave at the plane interface between vacuum and elastic solid [17].

The dispersion equation has finite number of real roots and infinite number of complex roots with $\mathrm{Re}\xi_n > 0$. Due to the factor $\sqrt{1-\xi^2}$ all real roots lie within the interval $0 < \xi \leqslant 1$. The real roots are obtained from Eq. (6) with "+" sign in the right-hand side. Each complex root gives rise to an inhomogeneous plane wave in the expansions (3). These terms oscillate and decay with the coordinate z. For complex roots the decrements ν_n and η_n acquire imaginary parts, which must be negative in order for the corresponding modes to run *away* from the channel. This scattering condition is satisfied for the roots with $\mathrm{Im}\xi_n < 0$, which are obtained from Eq. (6) with "−" sign in the right-hand side. For each frequency ω all the real roots must be included in the expansions (3). The number of complex roots included in numerical calculations depends on desired accuracy. The roots are arranged in ascending order of the imaginary part of the longitudinal wave vector $\beta_n = \omega/(c_t\xi_n)(|\mathrm{Im}\beta_{n-1}| < |\mathrm{Im}\beta_n|)$, since those with smaller $|\mathrm{Im}\beta|$ give larger contributions. For infinitely long channel the complex solutions should be ignored as they decay exponentially with length, but they play an essential role in sound transmission through a finite-length channel.

Solutions of the transcendental equation (6) are obtained numerically. For channel of width d Eq. (6) gives implicit relation between the dimensionless phase velocity ξ and frequency ω. Substituting $\omega = (c_t/d)\xi q$, where $q = \beta d$ is dimensionless wave vector, into the argument of cotangent in Eq. (6), we obtain an equation which relates the dimensionless phase velocity ξ and wave vector q. This equation is independent of the channel width d and it leads to the spectrum shown in Fig. 2. The spectrum consists of two unequal parts. One is so-called *fast mode* propagating faster than sound wave in the fluid, $\xi > c_f/c_t$. It has an infinite number of branches (shown in red) which originate from the symmetric waveguide modes

$$\omega_n = c_f\sqrt{\left(\frac{2\pi n}{d}\right)^2 + \beta^2}, \quad n = 0,1,2,\ldots \tag{7}$$

of a channel with ideally rigid walls, $\rho_m, c_t \to \infty$. More detailed analysis of the spectrum in the limit $\rho_f/\rho_m \to 0$ is given in Appendix A. All the branches of the fast mode lie between two horizontal lines, $c_f/c_t < \xi \leqslant 1$. Unlike the waveguide spectrum (7) where each phase velocity ω_n/β diverges at $\beta = 0$, except the mode with $n = 0$, in a channel with elastic boundaries all fast modes start with finite phase

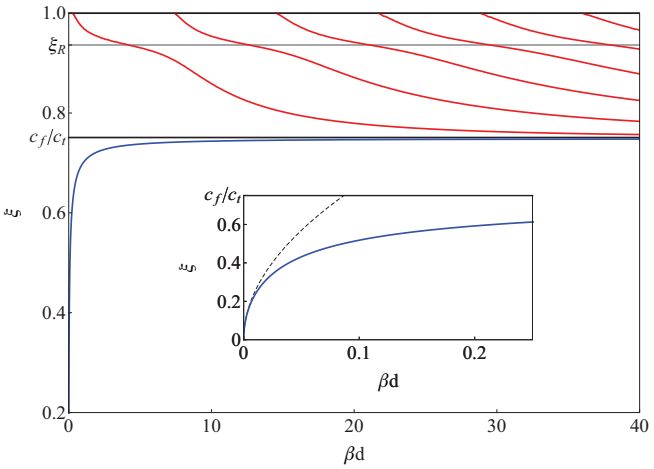

FIG. 2. (Color online) Dimensionless phase velocity $\xi = \Omega/q$ vs wave vector $q = \beta d$ for infinite brass channel filled by water. Fast mode is presented by infinite number of waveguide branches above the speed of sound in water, $c_f/c_t < \xi < 1$ (red curves). Phase velocity of the slow mode grows very fast (blue line near the vertical axis) and saturates at the level $\xi = c_f/c_t$ for very small $q = \beta d \approx 0.2$. Inset is the blowup of this narrow region where the phase velocity behaves as $\xi \sim \sqrt{qd}$. Dashed line is asymptotic dependence obtained from Eq. (9).

velocity $\xi = 1$ at the wave vector

$$Q_n = \beta_n d = \frac{2}{\sqrt{(c_t/c_f)^2 - 1}} \times \left[\pi n + \arctan\left(\frac{\rho_f}{\rho_m}\sqrt{\frac{1-(c_t/c_l)^2}{(c_t/c_f)^2-1}}\right)\right], \quad (8)$$
$$n = 0,1,2,\ldots.$$

Near the point where each branch crosses the level of the phase velocity of the Rayleigh wave, $\xi = \xi_R$, the slope of the dispersion curve noticeably decreases since for the parameters used in the plot of Fig. 2 the ratio $\rho_f/\rho_m = 0.12$ is quite small.

Another part of the spectrum in Fig. 2 is represented by a blue line. It is displaced below the level $\xi = c_f/c_t$, i.e., this mode propagates slower than sound in the fluid. The right-hand side of the dispersion equation (6) remains real, while the square root $\sqrt{(\frac{c_t}{c_f})^2\xi^2 - 1}$ is pure imaginary. The phase velocity of this mode grows extremely fast, starting from zero and approaching c_f for $q > 5$. The growth occurs in the subwavelength region, where the wavelength $\lambda = 2\pi/\beta = 2\pi d/q$ is greater than the channel width, $\lambda \geqslant 2\pi d/5$. This narrow subwavelength region is zoomed in the inset to Fig. 2. Within this region the frequency Ω and wave vector q are small parameters. Expansion of Eq. (6) leads to the following nonlinear dispersion in the low-frequency limit:

$$\Omega \approx \sqrt{\frac{\rho_m}{\rho_f}\left(1 - \frac{c_t^2}{c_l^2}\right)}(\beta d)^{3/2}. \quad (9)$$

As shown in Fig. 2, this asymptotics is valid in the region of very long wavelengths, when $\lambda > 100\pi d$. It is this part of the spectrum which provides penetration of sound through *any* narrow slit. Unlike transmission through a channel with ideally rigid walls where the dispersion is linear [see Eq. (7) for $n = 0$], in a real channel the vibrations of the walls result in nonlinear dispersion (9) with vanishing phase and group velocities in the low-frequency limit. Analysis of transmission through a subwavelength acoustic channel will be published elsewhere. It is noteworthy to mention that transmission of electromagnetic waves through a deeply subwavelength metallic slit also exhibits interesting features, which do not exist for perfectly conducting screens [27,28].

IV. SOLUTION OF THE SCATTERING PROBLEM

The eigenvalue problem which leads to the dispersion equation (6) also gives the relations between the coefficients $l_n^{\pm}$, $s_n^{\pm}$, and $b_n^{\pm}$:

$$l_n^{\pm} = -\frac{ik_n c_t^2}{\nu_n \omega^3}\left(\eta_n^2 + \beta_n^2\right)\sin\frac{k_n d}{2} e^{\nu_n d/2} b_n^{\pm},$$
$$s_n^{\pm} = -\frac{2k_n \beta_n c_t^2}{\omega^3}\sin\frac{k_n d}{2} e^{\eta_n d/2} b_n^{\pm}. \quad (10)$$

These relations are obtained from the linear set (A3). Using Eq. (10) the coefficients $l_n^{\pm}$ and $s_n^{\pm}$, which define the fields in the solid plates, can be eliminated and the unknowns left are $t(k)$, $r(k)$, and $b_n^{\pm}$. These four unknowns are calculated from four boundary conditions for velocity and pressure at two vertical boundaries, $x = 0$ and $x = h$:

$$(p_0/i\omega\rho_f) + R(x=0,z) = B(x=0,z), \quad |z| < d/2,$$
$$p_0 - i\omega\rho_f R(x=0,z) = \sigma_{xx}(x=0,z), \quad |z| > d/2, \quad (11)$$

$$\frac{p_0}{\rho_f c_f} + \frac{\partial R(x,z)}{\partial x}|_{x=0} = \frac{\partial B(x,z)}{\partial x}|_{x=0}, \quad |z| < d/2,$$
$$\frac{p_0}{\rho_f c_f} + \frac{\partial R(x,z)}{\partial x}|_{x=0} = -i\omega u_x(x=0,z), \quad |z| > d/2, \quad (12)$$

$$T(x=h,z) = B(x=h,z), \quad |z| < d/2,$$
$$-i\omega\rho_f T(x=h,z) = \sigma_{xx}(x=h,z), \quad |z| > d/2, \quad (13)$$

$$\frac{\partial T(x,z)}{\partial x}|_{x=h} = \frac{\partial B(x,z)}{\partial x}|_{x=h}, \quad |z| < d/2,$$
$$\frac{\partial T(x,z)}{\partial x}|_{x=h} = -i\omega u_x(x=h,z), \quad |z| > d/2. \quad (14)$$

Although there are formally eight equations and only four unknowns, the system is not overdetermined. In fact, each pair of equations defines one of the physical parameters—stress/pressure or velocity—at the semiaxis $z > 0$, which is divided into two intervals occupied by fluid, $0 < z < d/2$, and metal, $d/2 < z < \infty$. Thus the number of independent equations is four.

Substitution of the explicit expressions (1), (2), and (3) for the potentials $R(x,z)$, $T(x,z)$, and $B(x,z)$ into Eqs. (11)–(14) leads to a set of linear equations for two unknown continuous functions, $t(k)$ and $r(k)$, and two discrete unknowns, $b_n^{\pm}$; see Eqs. (B1)–(B4) in Appendix B. Two functions, $r(k)$ and $t(k)$, can be eliminated analytically and for the remaining two unknowns, $b_n^{\pm}$, a set of linear equations is obtained (B11)–(B12), which is solved numerically. Derivation of the set of equations for $b_n^{\pm}$ given in Appendix B is complicated by nonorthogonality of the eigenfunctions used in the expansions (3). It is well known that an eigenvalue problem for elastic waves in a finite volume leads to a set of nonorthogonal eigenfunctions. In particular, normal vibrations of elastic plate (Lamb waves) are not orthogonal over the width of the plate [29]. While several "orthogonality relations" for Lamb waves based on the reciprocity relations have been proposed [19,30], they (or their modification for solid-fluid structure [31]) cannot help in calculation of $b_n^{\pm}$. In Appendix B we use a basis of trigonometric functions for derivation of the linear set of equations for $b_n^{\pm}$. Once the coefficients $b_n^{\pm}$ are known, then the Fourier components $r(k)$ and $t(k)$ can be calculated that give the solution of the scattering problem in the form of integrals (1), (2).

V. TRANSMISSION, REFLECTION, AND REDIRECTION OF SOUND

The proposed method of calculation of transmitted and reflected acoustic fields excited by a plane wave is practically exact. The only physical approximations we used—the linear Hooke's Law and inviscid fluid—do not really affect the accuracy of the obtained results. Indeed, the width of the

viscous boundary layer $\sqrt{2\nu/\omega} \approx 10^{-4}$ cm in water ($\nu = 0.01$ cm^2/s) is negligible as compared with the apertures used in our experiments. Therefore, the calculated spectra of *direct* transmission

$$\mathcal{T}_\parallel(\omega) = \frac{1}{A p_0 v_{0x}} \int_A I_\parallel(x=l,z)dy\,dz$$
$$= \frac{1}{\pi R_d^2 p_0 v_{0x}} \int_{-R_d}^{R_d} I_\parallel(x=l,z)\sqrt{R_d^2 - z^2}dz \quad (15)$$

are in excellent agreement with the experimental spectra, as shown in Fig. 1. Here $A = \pi R_d^2$ is the area of the transducer antenna, $l = 8$ cm is the coordinate of the receiver, $p_0 v_{0x}$ is the flux in the incident wave, and $I_\parallel = p(x,z)v_x^*(x,z) = i\omega\rho_f T(x,z)[\partial T^*(x,z)/\partial x]$ is parallel to the channel component of the transmitted flux of sound energy. Note that no fitting parameters were used in the plots. The agreement is observed within a wide range of frequencies, for different metal plates (aluminum and brass), and for very different geometry of the slit: short and wide channel, $h < d$, Figs. 1(a) and 1(b), and long and narrow channel, $d < h$, Figs. 1(c) and 1(d).

The accuracy of the theoretical spectra depends on the number of complex roots of Eq. (6) included in the expansions (3). To plot the transmission spectra in Fig. 1 we numerically calculated each root as a function of frequency, i.e., each root generates a trajectory $\xi_n(\omega)$ in the complex ξ plane (see Fig. 8). The convergence of the series (3) is slower for wider channels; therefore, in calculations of the results shown in Figs. 1(a) and 1(b) the number of complex roots was 11, while the plots in Figs. 1(c) and 1(d) were obtained with only 7 complex roots. For all the graphs addition of one more complex root leads to less than 1% variation. As in any waveguide the number of real roots (propagating modes) increases with frequency, i.e., each new real root emerges at cutoff frequency, except the slow mode which starts from zero frequency. For the fast mode the cutoff frequencies $Q_n c_t/d$ are obtained from Eq. (8). For the frequencies near 1.4 MHz Eq. (6) has 8, 5, 2, and 2 real roots for the channels whose spectra are shown in Figs. 1(a)–1(d). One of these running modes is always the slow mode. In the case of brass channel the cutoff frequency for the second ($n = 1$) waveguide mode $Q_1 c_t/d = 2.35$ MHz for the channel with width $d = 1$ mm. Therefore, it does not contribute to sound transmission in our experiments. Its contribution becomes essential for width $d > 2$ mm.

In order to analyze the physical nature of the deep minima in Fig. 1, we calculated the reflection spectrum for the slit with $h = 3$ mm and $d = 0.5$ mm and plotted it in Fig. 3 together with the total transmission $T_\parallel$ through the whole boundary $x = h$.

The positions of the minima in the reflection in Fig. 3(a) coincides with the positions of the minima in the transmission in Fig. 1(c). Near these minima the sum of forward and backward scattered flux, $T_\parallel + R$, is considerably less than 1; that is a clear indication that this sum does not represent the total flux scattered by the slit. Since the slit shown in Fig. 1 is a 2D scattering system, the lack of scattered flux, $1 - T_\parallel - R$, is the energy scattered along axis z. In Fig. 3(b) we plot the spectrum transmitted from the fluid to the metal through the horizontal boundary $z = d/2$. It exhibits maxima exactly at the frequencies where $T_\parallel + R$ exhibits minima, thus representing

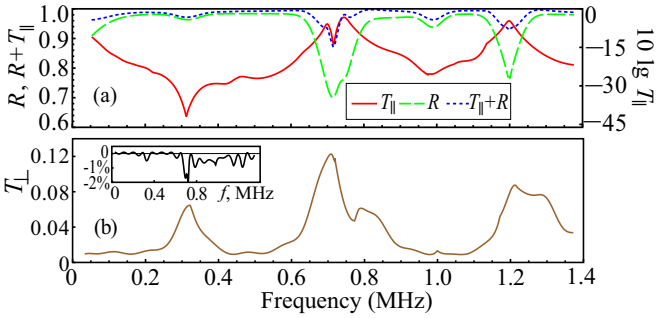

FIG. 3. (Color online) Calculated transmission and reflection spectra for two square brass plates with sides of length $L = 12$ cm separated by a slit with $h = 3$ mm and $d = 0.5$ mm. The measured transmission spectrum is shown in Fig. 1(c). (a) Transmission through the whole vertical boundary $x = h$ (solid-red line), $T_\parallel = C\int_0^{L+d/2} T(h,z)\frac{\partial T^*(x,z)}{\partial x}|_{x=h}\,dz$. Log scale for $T_\parallel$ is displaced on the right. Reflection from the whole vertical boundary $x = 0$ (long dashed-green line), $R = C\int_0^{L+d/2} R(0,z)\frac{\partial R^*(x,z)}{\partial x}|_{x=0}\,dz$, and the sum $T_\parallel + R$ (short dashed-blue line). (b) Transmission $T_\perp = C\int_0^h B(x,d/2)\frac{\partial B^*(x,z)}{\partial z}|_{z=\frac{d}{2}}\,dx$ through the horizontal boundary $z = d/2$. Inset demonstrates conservation of energy: the deviation of the sum $T_\parallel + T_\perp + R$ from 1 does not exceed 2%. $C = i\omega\rho_f^2 c_f/(p_0^2 L)$ is the normalization constant.

the flux, $T_\perp$, which is lost if the slit is approximated as a 1D scatterer. The total scattered flux $T_\parallel + T_\perp + R$, which fluctuates due to numerical errors, still remains very close to 1, as shown in the inset to Fig. 3(b).

Vibrations of the metal-fluid boundary $z = \pm d/2$ break 1D symmetry of the system, i.e., these boundaries are not flat any more. This broken symmetry of the channel boundaries gives rise to the elastic wave propagating in the metal plates perpendicular to the incident wave. The flux of energy $T_\perp$ associated with this redirected wave does not appear in the model of rigid screen which was accepted in many previous studies. Therefore, the property of a slit to redirect the incoming flux into metal is manifested only for elastic screens. The amount of redirected acoustic energy may reach 12% at the frequencies near 0.7 MHz, as shown in Fig. 3. This is a relatively strong effect, taking into account that a brass plate in water transmits only about 8% (−11 Db) in the minimum of the Fabry-Pérot resonance.

Enhanced radiation of sound into metal occurs due to large amplitude of vertical vibrations u_z of the plate boundaries at $z = \pm d/2$. Suppressed direct transmission and reflection originate from low pressure $p(x,z)$ at the channel ends and also from small amplitude of horizontal vibrations u_x of the plate boundaries $x = 0$ and $x = h$. When these two effects occur at close frequencies they mutually enhance each other, leading to extraordinarily low transmission. The sharper a dip in Fig. 1, the more energy is redirected into metal. The sharpness of a dip depends on how close to zero the pressure $p(x,z)$ and the displacement u_x become at $x = 0,h$. Being represented by a sum of plane waves taken over the roots of the dispersion equation, these quantities become small when those plane waves that give the principal contribution interfere almost destructively at the length of the channel h. It may occur that another pair of eigenmodes with smaller amplitudes

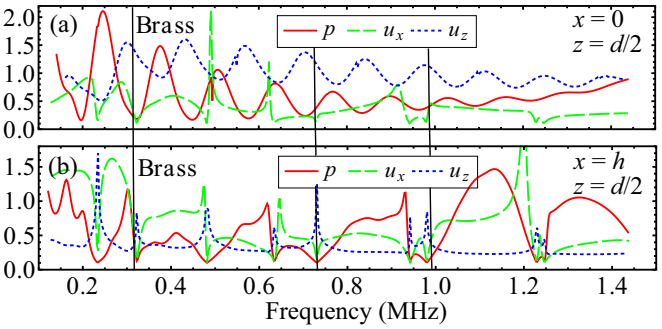

FIG. 4. (Color online) Frequency dependence of the pressure, horizontal, and vertical displacement of the plates at the left (a) and right (b) ends of the same channel as in Fig. 3. Straight vertical lines mark the positions of the deep minima in the transmission shown in Fig. 1(c).

also interfere destructively, thus leading to even sharper dip. It is, however, nearly impossible to predict how the amount of redirected energy depends on the geometry of the channel and frequency, since it depends on the values of the roots of the transcendental equation (6).

In Fig. 4 we plot the pressure and the amplitudes of horizontal and vertical vibrations at the channel ends ($x = 0, h$) vs frequency. It is clearly seen that near the resonant frequencies where minima in the transmission are experimentally observed (marked by vertical lines) the amplitude of horizontal vibrations of both faces of the plates is close to zero. The same is true for the pressure at the ends of the channel. Since the vibrations of the plates and the fluid are coupled through the boundary conditions, we conclude that a quasistanding wave is formed in the whole system due to interference between two eigenmodes propagating in opposite directions. At the same resonant frequencies the amplitude of the vertical vibrations reaches its local maxima that explains strong radiation into metal. While the graphs in Fig. 4 exhibit many peaks, strong redirection of sound occurs when minimum in pressure and displacement u_x coincides with maximum in displacement u_z. The depth and width of the minimum in $T_{\|}$ depends on how close to each other these three extrema occur. For example, the first two minima at 0.32 and 0.71 MHz in Figs. 1(c) and 3(a) are well pronounced since the frequencies of all three extrema practically coincide. Unlike this, the third minimum at 1 MHz is quite broad due to visible shifts in the positions of the extrema. There are two Fabry-Pérot resonances at 0.72 and 1.22 MHz in the transmission spectrum in Fig. 1(c). Here the situation is quite simple and standard—maximum in transmission coincides with minimum in reflection. This also can be seen from Fig. 4(b) where the amplitude of longitudinal vibrations at the right face ($x = h$) of the plate exceeds that on the left face ($x = 0$), especially for the resonance at 1.22 MHz which is not affected by close proximity of a deep minimum in transmission.

In Fig. 1(c) two minima at 0.32 and 0.71 MHz in transmission are associated with appearance of the real roots of Eq. (6), $\xi_1 = 0.99$ and $\xi_2 = 0.715$, respectively. The first root corresponds to excitation of the fast mode, since its phase velocity $c_t\xi_1$ exceeds the speed of sound in the fluid c_f. For the second root, ξ_2, the phase velocity of the corresponding eigenmode is less than c_f; therefore, this minimum is due to excitation of the slow mode. The minima associated with excitation of the slow mode are marked by arrows in the transmission spectra shown in Fig. 1. As a rule, these minima are sharp and asymmetric, except the minimum at 0.4 MHz in Fig. 1(d), the structure of which is strongly affected by a standard Fabry-Pérot resonance.

VI. NUMERICAL MODELING BY FINITE ELEMENT METHOD

Theoretical and experimental results are also supported by finite element simulations, which were performed through the commercially available software Comsol Multiphysics. The employed model is represented in Fig. 5. It consists of a two-dimensional domain filled with a fluid having the acoustic properties of water. Two elastic plates with thickness h and separated by a distance d are displaced forming a fluid channel. The plates are of the same length of 12 cm as the experimental samples. At the ends both plates terminate with two additional absorbing domains [or elastic perfectly matched layers (PML)] in order to suppress reflection. Normally incident Gaussian beam is used as impinging wave to provide a more realistic excitation. The exterior boundaries of the model are configured with nonreflecting conditions, ensuring that outgoing waves leave the domain.

A frequency sweep is performed numerically for different thicknesses h and apertures d of the slit. This process provides

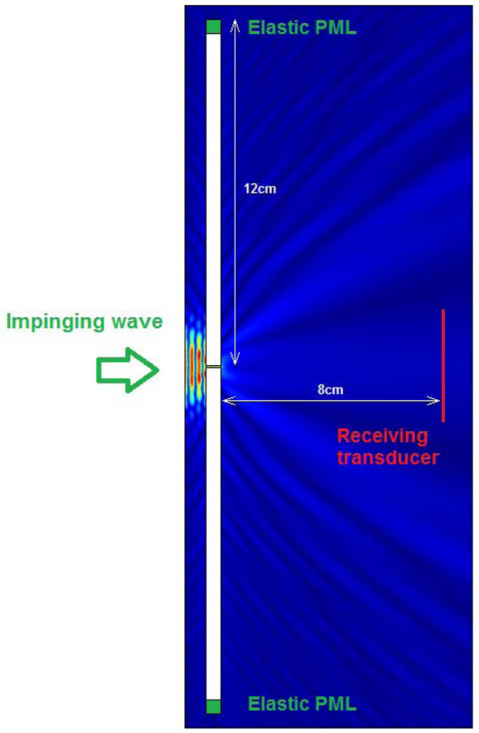

FIG. 5. (Color online) Structure of the fluid channel used for numerical simulations. A Gaussian beam coming from the left impinges on the slit and the pressure field is obtained behind the plates. The illustrated pattern corresponds to two brass plates with $h = 5$ mm, $d = 1$ mm at frequency 0.32 MHz.

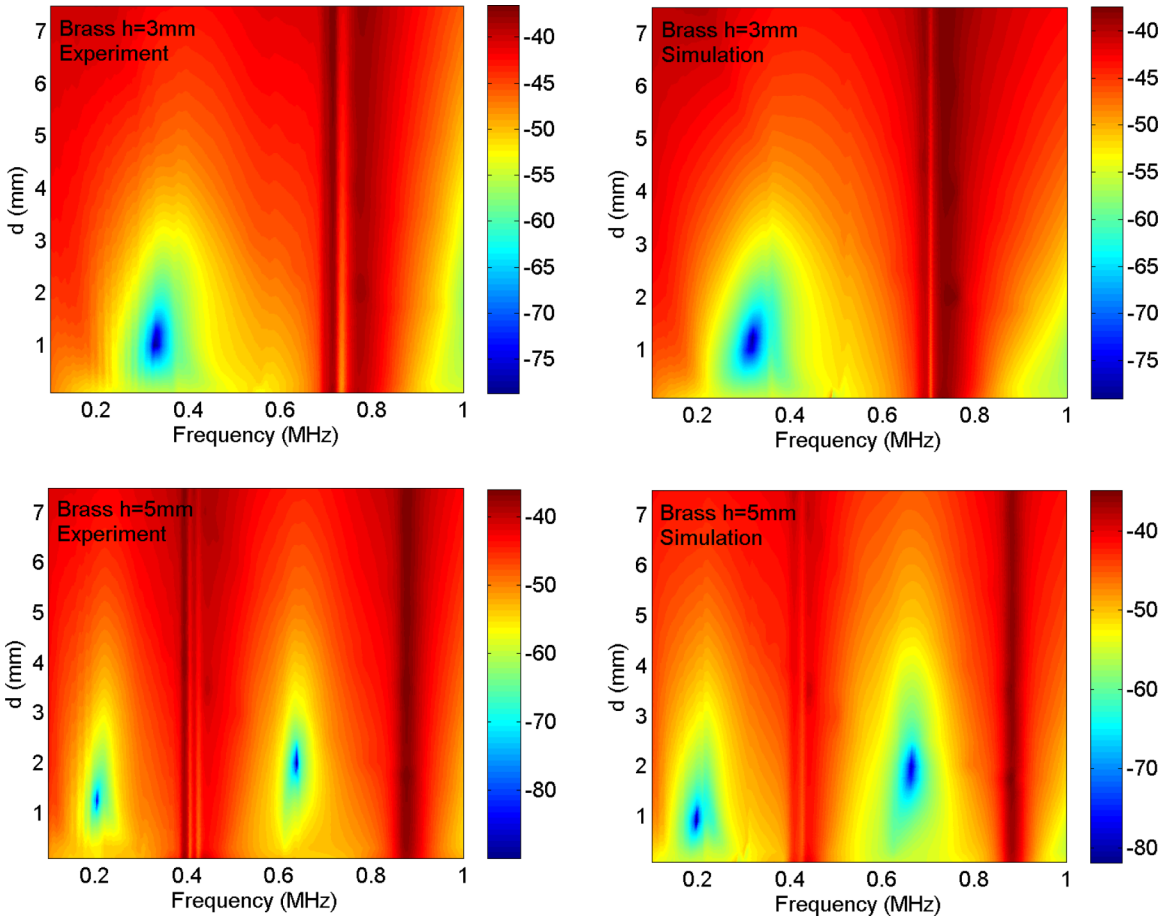

FIG. 6. (Color online) Transmitted pressure at the receiving antenna (in dB) for a slit between two brass plates with $h = 3$ mm (top) and $h = 5$ mm (bottom) at several apertures and frequencies. Left (right) panels correspond to experimental (simulated) data.

a large amount of data which can be summarized through maps showing the transmitted pressure as a function of frequency and aperture. In addition, the same sweep was also experimentally carried out using an automated setup. In Fig. 6 we compare experimental and numerical data for brass plates with thicknesses $h = 3$ mm and $h = 5$ mm. The numerical data are obtained by integrating the pressure field over the length of the receiving transducer (see Fig. 5). Both maps exhibit regions of parameters with anomalously low transmission. There is excellent agreement between the positions of the deep minima obtained experimentally, theoretically, and numerically. The deepest minima at 0.32 MHz for $h = 3$ mm and at 0.2 and 0.64 MHz for $h = 5$ mm appear as bright blue spots in the maps in Fig. 6. Unlike this, less deeper minima at 0.71 MHz ($h = 3$ mm) and at 0.4 MHz ($h = 5$ mm) appear as narrow yellow lines on red background. This occurs because these local minima are close to the maxima of the Fabry-Pérot resonances. These less-deeper minima correspond, as it is explained in the main text, to excitation of the slow mode. The minimum at 0.4 MHz ($h = 5$ mm) has a doublet structure [see Fig. 1(d)], which is well reproduced in the experimental map in Fig. 6. It, however, is not resolved in our numerical simulations. It is worth mentioning that no viscosity effects were considered in the fluid, thus demonstrating that the reported effects are not due to viscous phenomena inside the channel.

The elastic displacements were also obtained from the simulations, allowing the observation of the wave phenomena occurring inside the plates. A motion picture showing the pressure map in the fluid superimposed with the lines of displacement (either in water or metal) is presented in the Supplemental Material Movie S1 [32]. It is calculated for brass plates with $h = 3$ mm and $d = 0.5$ mm [the same parameters as in Fig. 1(c)] at 0.704 MHz. It is shown how the incoming wave generates elastic vibrations inside the slit and the plates and how these vibrations propagate. It is easy to see that the vibrations of the plate which originally are localized near the channel boundaries become leaky modes, carrying the acoustic energy away from the channel in a form of vortices. The vortex structure of the displacement field in metal is due to nonpotential contribution $\nabla \times S$ to the displacement field $\mathbf{u}$. This movie visualizes the effect of redirection of sound by a straight fluid channel with elastic boundaries.

VII. SUMMARY

In summary, we reported a comprehensive study of sound transmission through a finite-length fluid channel with elastic boundaries. It is experimentally observed and explained how a straight fluid slit between two metallic screens may serve as a redirecting acoustic antenna. This previously unknown property is due to excitation and interference of the

eigenmodes which describe the synchronized vibrations of the fluid and metal plates. The proposed method of solution of the scattering problem for a slit is practically exact and leads to excellent agreement with the experiment. The proposed analytical approach may be easily extended to more complicated geometries, in particular, to a set of periodically arranged slits. The effect of redirection of sound may find applications in design of specific devices for manipulation of acoustic energy and vibration of plates embedded into fluids. The resonant modes which are responsible for the redirection of sound are of particular interest for microfluidics since pressure produced by the vibrating boundaries is comparable with the capillarity force or the force generated by a micropump.

ACKNOWLEDGMENTS

This study is supported by the Office of Naval Research (USA) under Contract No. N00014-12-1-0216. A.K. acknowledges support from the program "Plan de Movilidad e Internalización Academica VLC/CAMPUS."

APPENDIX A: DERIVATION OF THE DISPERSION RELATION

Consider a monochromatic sound wave propagating along an infinite straight fluid channel clad between two elastic plates. A solution of the wave equation in the fluid and in the plates can be written as a superposition of the corresponding eigenmodes Eq. (3). Linear relations between the coefficients b_n, l_n, and s_n are obtained from the boundary conditions. Since the channel is infinite we can consider only the waves propagating in positive direction of axis x and omit superindices $\pm$.

At the fluid-metal interface $z = d/2$ the stress and the normal component of the velocity are continuous

$$\sigma_{zz} = -p, \quad \sigma_{xz} = 0, \quad \dot{u}_z = v_z. \tag{A1}$$

Here $\sigma_{ik}(x,z)$ is the stress tensor in the elastic plates. Using Hooke's Law $\sigma_{ik} = \lambda u_{ik} + \mu u_{ll}\delta_{ik}$ the nonzero components of the stress tensor can be expressed through the potentials

$$\begin{aligned}
\sigma_{xx} &= -\lambda k_l^2 L + 2\mu\left(\frac{\partial^2 L}{\partial x^2} - \frac{\partial^2 S}{\partial x \partial z}\right),\\
\sigma_{zz} &= -\lambda k_l^2 L + 2\mu\left(\frac{\partial^2 L}{\partial z^2} + \frac{\partial^2 S}{\partial x \partial z}\right),\\
\sigma_{xz} &= \mu\left(2\frac{\partial^2 L}{\partial x \partial z} + \frac{\partial^2 S}{\partial x^2} - \frac{\partial^2 S}{\partial z^2}\right).
\end{aligned} \tag{A2}$$

Here λ and μ are the Lamé coefficients, $\mu = \rho_m c_t^2$ and $\lambda + 2\mu = \rho_m c_l^2$. Substituting the potentials (3) to Eqs. (A2) and (4), the components of σ_{ik} and $\mathbf{u}$ are expressed through the unknown constants l_n and s_n. The velocity $\mathbf{v} = \nabla B$ and the pressure $p = i\omega\rho B$ are expressed through b_n. Thus all the dynamical variables are given in terms of three unknowns, l, s, and b.

The boundary conditions Eq. (A1) written in terms of l, s, and b (here subindex n can be omitted) lead to the following set of linear equations:

$$\begin{aligned}
&\left(2\mu\nu^2 - \lambda k_l^2\right) e^{-\nu d/2} l\\
&\quad - 2i\mu\eta\beta\, e^{-\eta d/2} s + i\omega\rho_f \cos(kd/2) b = 0,\\
&2i\nu\beta\, e^{-\nu d/2} l + e^{-\eta d/2}\left(\beta^2 + \eta^2\right) s = 0,\\
&k\, \sin(kd/2) b + i\omega\nu\, e^{-\nu d/2} l + \omega\beta\, e^{-\eta d/2} s = 0.
\end{aligned} \tag{A3}$$

This set has nontrivial solution if the corresponding determinant vanishes, viz,

$$(\eta^2 + \beta^2)^2 - 4\nu\eta\beta^2 = \frac{\rho_f}{\rho_m}\frac{\omega^4}{c_t^4}\frac{\nu}{k}\cot\frac{kd}{2}. \tag{A4}$$

Here k, ν, and η are expressed through ω and β using Eq. (5). Dependence on the channel width d can be eliminated if dimensionless frequency $\Omega = \omega d/c_t$ and wave vector $q = \beta d$ are introduced:

$$\begin{aligned}
&(2q^2 - \Omega^2)^2 - 4q^2\sqrt{q^2 - (c_t/c_l)^2\Omega^2}\sqrt{q^2 - \Omega^2}\\
&= \frac{\rho_f}{\rho_m}\Omega^4\sqrt{\frac{q^2 - (c_t/c_l)^2\Omega^2}{(c_t/c_f)^2\Omega^2 - q^2}}\cot\left(\frac{1}{2}\sqrt{\frac{c_t^2}{c_f^2}\Omega^2 - q^2}\right).
\end{aligned} \tag{A5}$$

Dispersion relation (6) for the phase velocity ξ is obtained from Eq. (A5) by substitution $q = \Omega/\xi$. Real and complex solutions of Eq. (A5) define the allowed values of the wave vector $q_n = q_n(\Omega)$ for each frequency Ω.

The structure of the spectrum given by Eq. (A4) is shown in Fig. 7. The dimensionless frequency is plotted versus $kd/2$. Since k is not the wave vector in the direction of propagation, the slope of the curves is not related to the phase velocity. For almost all values of $kd/2$ the right-hand side of Eq. (A4) can

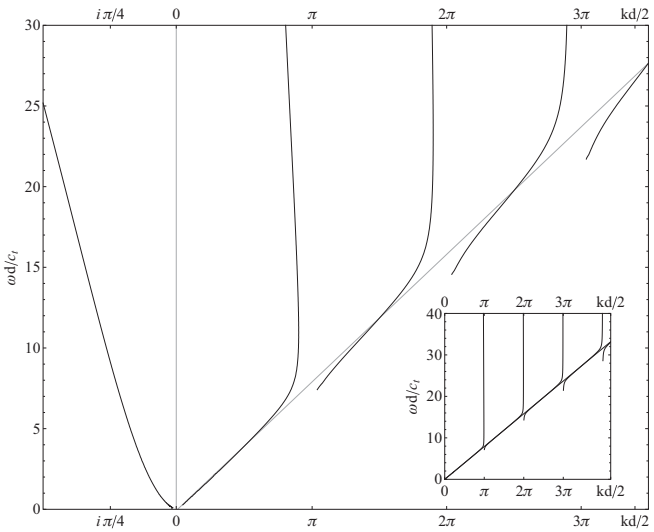

FIG. 7. Dispersion relation between dimensionless frequency $\Omega = c_t\omega/d$ and transverse wave vector $kd/2$ obtained from Eq. (A4) for infinite brass channel filled by water, $\rho_f/\rho_m = 0.12$. Linear dispersion for the case $\rho_f/\rho_m = 0$ (Rayleigh wave) is shown by thin line. Inset shows the dispersion of the fast mode for very weak coupling, $\rho_f/\rho_m = 0.01$. In this case the waveguide modes are reduced to almost vertical lines at $kd/2 = \pi n$. Dispersion of the slow mode obtained from Eq. (A4) for pure imaginary values of k is plotted to the left of the origin.

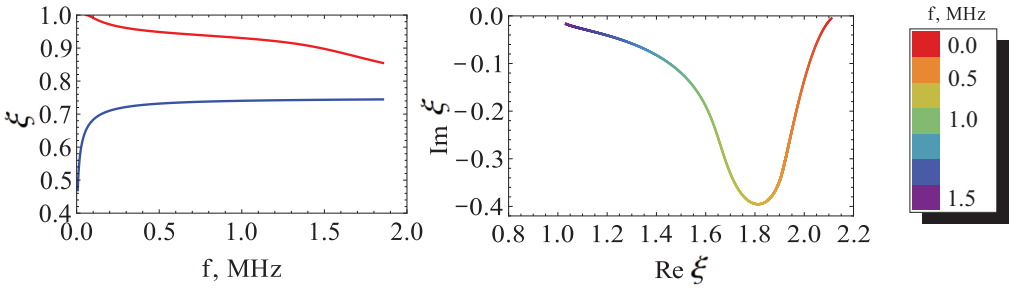

FIG. 8. (Color online) Left panel: frequency dependence of the first two real roots of the dispersion equation (A4) for water channel between two brass plates. Right panel: trajectory of the first complex root for the same system.

be neglected since $\rho_f/\rho_m \ll 1$. In this approximation Eq. (A4) gives linear dispersion (Rayleigh wave) which serves as asymptote for the dispersion curves of the fast mode. However, near the points where $kd/2 = \pi n$ ($n = 1,2,\dots$) the Rayleigh wave becomes a waveguide mode of a channel with rigid walls. Here the dispersion curves become practically vertical lines as a result of quantization condition $v_z = \frac{\partial B}{\partial z}|_{z=\pm d/2} = 0$. For very small ratio $\rho_f/\rho_m = 0.01$ the spectrum exhibits this quantization condition with high accuracy, as one can see in the inset to Fig. 7. The slow mode corresponds to pure imaginary values of k in Eq. (A4). In Fig. 7 these values are plotted along the negative direction of the horizontal axis. At $kd/2 \gg 1$ the dispersion of the slow mode becomes linear since $\coth(kd/2) \to 1$ and Eq. (A4) is reduced to a polynomial equation over ω/k. The tendency to linear dispersion is manifested as saturation of the phase velocity in Fig. 2.

Expansions (3) of the potentials over eigenmodes can be used if all real roots and sufficient number of complex roots of the dispersion equation (6) are known. In the general case each root depends on frequency, $\xi_n = \xi_n(\omega)$, that shows frequency dispersion of the corresponding mode. Examples of frequency dispersion for the lowest two real solutions are given in the left panel in Fig. 8. The mode which starts at $\omega = 0$ is the slow mode (blue line). It exhibits strong dispersion in the subwavelength regime and at $\omega > 0.5$ MHz the phase velocity saturates at the level $\xi = c_f/c_t$, i.e., the slow mode becomes dispersionless sound wave, propagating with speed c_f. Red line shows dispersion of the first waveguide mode. This mode starts at cutoff frequency $(c_t/d)\Omega_1$. Frequency dispersion of a complex root can be visualized as a trajectory in complex plane. One of such trajectories is shown in the right panel in Fig. 8. This complex root has very small imaginary part at low frequencies. Therefore, it gives a contribution to subwavelength transmission which is comparative with the contribution of the pure real root which gives rise to the slow mode.

It is important to stress that the Fabry-Pérot maxima in transmission are due to the roots which are necessarily complex. Indeed, these maxima appear when longitudinal waves interfere constructively at the length h. Since $c_l > c_t$, the roots of the dispersion equation which correspond to the phase velocities close to c_l cannot lie within the interval $0 < \xi \leqslant 1$ (where all the real roots lie), i.e., they are all complex. This complexity reflects an obvious fact that in a solid plate with a slit pure longitudinal waves cannot propagate. The channel boundary gives rise to shear displacements which change the amplitude and phase of the Fabry-Pérot resonance. Nevertheless, the imaginary part of the quasilongitudinal solution may be quite small leading only to slight modification of the Fabry-Pérot resonance. For example, the complex root shown in Fig. 8 has the real part close to 2 (which is approximately the ratio c_l/c_t in brass) and negligible imaginary part in the limits of either zero frequency or zero channel width. This root corresponds to quasilongitudinal sound wave propagating in metal.

APPENDIX B: CALCULATION OF THE TRANSMISSION AND REFLECTION COEFFICIENTS

Substitution of the potential expansions (3) into the boundary conditions Eqs. (11)–(14) leads to the following set of linear equations:

$$\frac{p_0}{i\omega\rho_f} + \int_{-\infty}^{+\infty} r(k)e^{ikz}dk = \begin{cases} \sum_{n=1}^{\infty}(b_n^+ + b_n^-)\cos k_n z, & |z| < d/2, \\ \frac{1}{i\omega\rho_f}\sum_{n=1}^{\infty}(l_n^+ + l_n^-)\left(\lambda k_l^2 + 2\mu\beta_n^2\right)e^{-\nu_n|z|} - \frac{2\mu}{\omega\rho_f}\sum_{n=1}^{\infty}\eta_n\beta_n(s_n^+ + s_n^-)e^{-\eta_n|z|}, & |z| > d/2, \end{cases} \tag{B1}$$

$$\frac{p_0}{ic_f\rho_f} - \int_{-\infty}^{+\infty} r(k)\beta(k)e^{ikz}dk = \begin{cases} \sum_{n=1}^{\infty}(b_n^+ - b_n^-)\beta_n\cos k_n z, & |z| < d/2, \\ -i\omega\sum_{n=1}^{\infty}(l_n^+ - l_n^-)\beta_n e^{-\nu_n|z|} - \omega\sum_{n=1}^{\infty}(s_n^+ - s_n^-)\eta_n e^{-\eta_n|z|}, & |z| > d/2, \end{cases} \tag{B2}$$

$$\int_{-\infty}^{+\infty} t(k)e^{ikz}dk = \begin{cases} \sum_{n=1}^{\infty}(b_n^+e^{i\beta_n h} + b_n^-e^{-i\beta_n h})\cos k_n z, & |z| < d/2, \\ \frac{1}{i\omega\rho_f}\sum_{n=1}^{\infty}(l_n^+e^{i\beta_n h} + l_n^-e^{-i\beta_n h})\left(\lambda k_l^2 + 2\mu\beta_n^2\right)e^{-\nu_n|z|} \\ -\frac{2\mu}{\omega\rho_f}\sum_{n=1}^{\infty}\eta_n\beta_n(s_n^+e^{i\beta_n h} + s_n^-e^{-i\beta_n h})e^{-\eta_n|z|}, & |z| > d/2, \end{cases} \tag{B3}$$

$$\int_{-\infty}^{+\infty} t(k)\beta(k)e^{ikz}dk = \begin{cases} \sum_{n=1}^{\infty}(b_n^+ e^{i\beta_n h} - b_n^- e^{-i\beta_n h})\beta_n \cos k_n z, & |z| < d/2, \\ -i\omega\sum_{n=1}^{\infty}(l_n^+ e^{i\beta_n h} - l_n^- e^{-i\beta_n h})\beta_n e^{-\nu_n|z|} - \omega\sum_{n=1}^{\infty}(s_n^+ e^{i\beta_n h} - s_n^- e^{-i\beta_n h})\eta_n e^{-\eta_n|z|}, & |z| > d/2. \end{cases} \tag{B4}$$

The equations (B1)–(B4) form a linear set which, being inhomogeneous, has a unique solution. The inhomogeneous term in the LHS of Eqs. (B1) and (B2) is due to the incoming plane wave with the amplitude $p_0/(i\omega\rho_f)$. Using the linear relations (10), the unknowns $l_n^{\pm}$ and $s_n^{\pm}$ can be expressed through $b_n^{\pm}$. Then, the number of unknowns in Eqs. (B1)–(B4) is reduced to four: b_n^+, b_n^-, $r(k)$, and $t(k)$.

It is possible to reduce the number of unknowns analytically. This is easy to do since in the LHS of Eqs. (B1)–(B4) the unknowns $r(k)$ and $t(k)$ enter through their Fourier transformations. Applying the inverse Fourier transformation to Eqs. (B2) and (B4) (where $l_n^{\pm}$ and $s_n^{\pm}$ have already been expressed through $b_n^{\pm}$) we obtain the following formulas:

$$\begin{aligned} r(k) = &-\frac{p_0}{i\omega\rho_f}\delta(k) + \frac{1}{2\pi}\sum_{n=1}^{N}(b_n^+ + b_n^-)\left[\left(\frac{\sin[(k_n+k)d/2]}{k_n+k} + \frac{\sin[(k_n-k)d/2]}{k_n-k}\right)\right. \\ &- \frac{2k_n c_t^2}{\nu_n\omega^4\rho_f}\frac{\left(\eta k_l^2 + 2\mu\beta_n^2\right)\left(\eta_n^2+\beta_n^2\right)}{\nu_n^2+k^2}\sin(k_n d/2)\left[\nu_n\cos(kd/2) - k\sin(kd/2)\right] \\ &\left. + \frac{8\mu c_t^2}{\omega^4\rho_f}\frac{k_n\eta_n\beta_n^2}{\eta_n^2+k^2}\sin(k_n d/2)\left[\eta_n\cos(kd/2) - k\sin(kd/2)\right]\right], \end{aligned} \tag{B5}$$

$$\begin{aligned} t(k) = &\frac{1}{2\pi}\sum_{n=1}^{N}(b_n^+ e^{i\beta_n h} + b_n^- e^{-i\beta_n h})\left[\left(\frac{\sin[(k_n+k)d/2]}{k_n+k} + \frac{\sin[(k_n-k)d/2]}{k_n-k}\right)\right. \\ &- \frac{2k_n c_t^2}{\nu_n\omega^4\rho_f}\frac{\left(\eta k_l^2 + 2\mu\beta_n^2\right)\left(\eta_n^2+\beta_n^2\right)}{\nu_n^2+k^2}\sin(k_n d/2)\left[\nu_n\cos(kd/2) - k\sin(kd/2)\right] \\ &\left. + \frac{8\mu c_t^2}{\omega^4\rho_f}\frac{k_n\eta_n\beta_n^2}{\eta_n^2+k^2}\sin(k_n d/2)\left[\eta_n\cos(kd/2) - k\sin(kd/2)\right]\right]. \end{aligned} \tag{B6}$$

Equations (B5) and (B6) give $r(k)$ and $t(k)$ in terms of $b_n^{\pm}$. Substituting $r(k)$ and $t(k)$ into the remaining two equations (B1) and (B3) we come to two equalities for $b_n^{\pm}$ where both their sides are functions of the variable z:

$$\begin{aligned} &\frac{2p_0}{i\omega\rho_f} - \frac{1}{2\pi}\sum_{n=1}^{\infty}(b_n^+ - b_n^-)\int_{-\infty}^{+\infty}\frac{\beta_n}{\beta(k)}\left[\frac{\sin[(k_n+k)d/2]}{k_n+k} + \frac{\sin[(k_n-k)d/2]}{k_n-k}\right. \\ &\quad\left. - \frac{2k_n c_t^2\left(\eta_n^2+\beta_n^2\right)}{\nu_n\omega^2\left(\nu_n^2+k^2\right)}\sin\frac{k_n d}{2}\left(\nu_n\cos\frac{kd}{2} - k\sin\frac{kd}{2}\right) + \frac{4\eta_n k_n c_t^2}{\omega^2\left(\eta_n^2+k^2\right)}\sin\frac{k_n d}{2}\left(\eta_n\cos\frac{kd}{2} - k\sin\frac{kd}{2}\right)\right]e^{ikz}dk \\ &= \begin{cases} \sum_{n=1}^{\infty}(b_n^+ + b_n^-)\cos k_n z, & |z| < d/2, \\ -\sum_{n=1}^{\infty}\frac{k_n c_t^2}{\omega^4\rho_f}(b_n^+ + b_n^-)\sin\frac{k_n d}{2}\left[\frac{\eta_n^2+\beta_n^2}{\nu_n}\left(\lambda k_l^2 + 2\mu\beta_n^2\right)e^{-\nu_n(|z|-\frac{d}{2})} - 4\mu\eta_n\beta_n^2 e^{-\eta_n(|z|-\frac{d}{2})}\right], & |z| > d/2, \end{cases} \end{aligned} \tag{B7}$$

$$\begin{aligned} &\frac{1}{2\pi}\sum_{n=1}^{\infty}(b_n^+ e^{i\beta_n h} - b_n^- e^{-i\beta_n h})\int_{-\infty}^{+\infty}\frac{\beta_n}{\beta(k)}\left[\frac{\sin[(k_n+k)d/2]}{k_n+k} + \frac{\sin[(k_n-k)d/2]}{k_n-k}\right. \\ &\quad\left. - \frac{2k_n c_t^2\left(\eta_n^2+\beta_n^2\right)}{\nu_n\omega^2\left(\nu_n^2+k^2\right)}\sin\frac{k_n d}{2}\left(\nu_n\cos\frac{kd}{2} - k\sin\frac{kd}{2}\right) + \frac{4\eta_n k_n c_t^2}{\omega^2\left(\eta_n^2+k^2\right)}\sin\frac{k_n d}{2}\left(\eta_n\cos\frac{kd}{2} - k\sin\frac{kd}{2}\right)\right]e^{ikz}dk \\ &= \begin{cases} \sum_{n=1}^{\infty}(b_n^+ e^{i\beta_n h} + b_n^- e^{-i\beta_n h})\cos k_n z, & |z| < d/2, \\ -\sum_{n=1}^{\infty}\frac{k_n c_t^2}{\omega^4\rho_f}(b_n^+ e^{i\beta_n h} + b_n^- e^{-i\beta_n h})\sin\frac{k_n d}{2}\left[\frac{\eta_n^2+\beta_n^2}{\nu_n}\left(\lambda k_l^2 + 2\mu\beta_n^2\right)e^{-\nu_n(|z|-\frac{d}{2})} - 4\mu\eta_n\beta_n^2 e^{-\eta_n(|z|-\frac{d}{2})}\right], & |z| > d/2. \end{cases} \end{aligned} \tag{B8}$$

The right-hand sides of Eqs. (B7) and (B8) are presented in the form of expansions over eigenfunctions of vibrating fluid channel. These eigenfunctions are defined on the semiaxis $z > 0$. They are oscillating, $\cos(k_n z)$, within the channel, $0 < z < d/2$, and evanescent, $\exp(-\eta_n z)$, $\exp(-\nu_n z)$, inside the metal plates, $z > d/2$. These eigenfunctions, as well as the displacements and velocities defined by them, are not orthogonal. The lack of orthogonality is due to the boundary conditions at $z = \pm d/2$, explicitly containing the eigenvector β_n, as it was mentioned in Ref. [30] with respect to nonorthogonality of Lamb modes in a solid plate.

While the nonorthogonal basis does not allow analytical calculation of the unknowns $b_n^{\pm}$, it really does not impose additional difficulty in numerical calculation. On the contrary, standard orthogonalization of the basis of channel eigenfunctions will require

more numerical efforts than direct solution of the set of linear equations by the method shown below. Due to the fact that the size of the set of equations (B7) and (B8) is cut by the number of calculated roots $\xi_n(\omega)$, $n = 1,2,\ldots,N$, the necessary set of equations for $b_n^{\pm}$ can, for example, be obtained by equating the first N Fourier coefficients of the both sides of Eqs. (B7) and (B8). We introduce the finite Fourier transform defined on a segment $0 < z < R_d$

$$f(z) = \frac{F_0}{2} + \sum_{m=1}^{N-1} F_m \cos\left(\frac{\pi m}{R_d} z\right), \quad 0 < z < R_d, \tag{B9}$$

$$F_m = \frac{2}{R_d} \int_0^{R_d} f(z) \cos\left(\frac{\pi m}{R_d} z\right) dz, \tag{B10}$$

where R_d is a parameter which gives the width of the region along axis z where the acoustic fields are calculated. If we need to know the fields within the transducer, then R_d must be a bit larger than the radius of the transducer antenna. Applying the Fourier transform (B10) to the both sides of Eqs. (B7) and (B8) the following linear set of equations for $b_n^{\pm}$ is obtained:

$$\begin{aligned}
&\frac{2p_0}{i\omega\rho_f} R_d \delta_{m,0} - \frac{1}{2\pi} \sum_{n=1}^{N} (b_n^+ - b_n^-) \int_{-\infty}^{+\infty} \frac{\beta_n}{\beta(k)} \left[\frac{\sin[(k_n + k)d/2]}{k_n + k} + \frac{\sin[(k_n - k)d/2]}{k_n - k} - \frac{2k_n c_t^2 (\eta_n^2 + \beta_n^2)}{\nu_n \omega^2 (\nu_n^2 + k^2)} \sin\frac{k_n d}{2} \right. \\
&\quad \left. \times \left(\nu_n \cos\frac{kd}{2} - k \sin\frac{kd}{2} \right) + \frac{4\eta_n k_n c_t^2}{\omega^2 (\eta_n^2 + k^2)} \sin\frac{k_n d}{2} \left(\eta_n \cos\frac{kd}{2} - k \sin\frac{kd}{2} \right) \right] \left(\int_0^{R_d} e^{ikz} \cos\frac{\pi m z}{R_d} dz \right) dk \\
&= \sum_{n=1}^{N} (b_n^+ + b_n^-) \left[\left(\int_0^{d/2} \cos k_n z \cos\frac{\pi m z}{R_d} dz \right) - \frac{k_n c_t^2}{\nu_n \omega^4 \rho_f} (\eta_n^2 + \beta_n^2) (\lambda k_l^2 + 2\mu\beta_n^2) \sin\frac{k_n d}{2} \left(\int_{d/2}^{R_d} e^{-\nu_n(|z| - \frac{d}{2})} \cos\frac{\pi m z}{R_d} dz \right) \right. \\
&\quad \left. + \frac{4\mu\eta_n k_n \beta_n^2 c_t^2}{\omega^4 \rho_f} \sin\frac{k_n d}{2} \left(\int_{d/2}^{R_d} e^{-\eta_n(|z| - \frac{d}{2})} \cos\frac{\pi m z}{R_d} dz \right) \right], \quad m = 0,1,2,\ldots,N-1,
\end{aligned} \tag{B11}$$

$$\begin{aligned}
&\frac{1}{2\pi} \sum_{n=1}^{N} (b_n^+ e^{i\beta_n h} - b_n^- e^{-i\beta_n h}) \int_{-\infty}^{+\infty} \frac{\beta_n}{\beta(k)} \left[\frac{\sin[(k_n + k)d/2]}{k_n + k} + \frac{\sin[(k_n - k)d/2]}{k_n - k} - \frac{2k_n c_t^2 (\eta_n^2 + \beta_n^2)}{\nu_n \omega^2 (\nu_n^2 + k^2)} \sin\frac{k_n d}{2} \right. \\
&\quad \left. \times \left(\nu_n \cos\frac{kd}{2} - k \sin\frac{kd}{2} \right) + \frac{4\eta_n k_n c_t^2}{\omega^2 (\eta_n^2 + k^2)} \sin\frac{k_n d}{2} \left(\eta_n \cos\frac{kd}{2} - k \sin\frac{kd}{2} \right) \right] \left(\int_0^{R_d} e^{ikz} \cos\frac{\pi m z}{R_d} dz \right) dk \\
&= \sum_{n=1}^{N} (b_n^+ e^{i\beta_n h} + b_n^- e^{-i\beta_n h}) \left[\left(\int_0^{d/2} \cos k_n z \cos\frac{\pi m z}{R_d} dz \right) - \frac{k_n c_t^2}{\nu_n \omega^4 \rho_f} (\eta_n^2 + \beta_n^2) (\lambda k_l^2 + 2\mu\beta_n^2) \sin\frac{k_n d}{2} \right. \\
&\quad \left. \times \left(\int_{d/2}^{R_d} e^{-\nu_n(|z| - \frac{d}{2})} \cos\frac{\pi m z}{R_d} dz \right) + \frac{4\mu\eta_n k_n \beta_n^2 c_t^2}{\omega^4 \rho_f} \sin\frac{k_n d}{2} \left(\int_{d/2}^{R_d} e^{-\eta_n(|z| - \frac{d}{2})} \cos\frac{\pi m z}{R_d} dz \right) \right], \quad m = 0,1,2,\ldots,N-1.
\end{aligned} \tag{B12}$$

This $2N \times 2N$ set of linear equations is solved numerically. Once $b_n^{\pm}$ are known, the reflection and transmission coefficients are calculated directly from Eqs. (B5) and (B6).

[1] J. W. S. Rayleigh, Proc. London Math. Soc. **17**, 4 (1885).
[2] R. D. Spence, J. Acoust. Soc. Am. **20**, 380 (1948).
[3] L. E. Kinsler, A. R. Frey, A. B. Coppens, and J. V. Sanders, *Fundamentals of Acoustics* (John Wiley & Sons, New York, 1982).
[4] G. P. Wilson and W. W. Soroka, J. Acoust. Soc. Am. **37**, 286 (1965).
[5] S. Tinti, J. Acoust. Soc. Am. **65**, 888 (1979).
[6] J. Christensen, L. Martin-Moreno, and F. J. García-Vidal, Phys. Rev. Lett. **101**, 014301 (2008).
[7] M.-H. Lu, X.-K. Liu, L. Feng, J. Li, C.-P. Huang, Y.-F. Chen, Y. Y. Zhu, S.-N. Zhu, and N.-B. Ming, Phys. Rev. Lett. **99**, 174301 (2007).
[8] T. W. Ebbesen, H. J. Lezec, H. F. Ghaemi, T. Thio, and P. A. Wolff, Nature (London) **391**, 667 (1998).
[9] L. Kelders, J. F. Allard, and W. Lauriks, J. Acoust. Soc. Am. **103**, 2730 (1998).
[10] X. Zhang, Phys. Rev. B **71**, 241102(R) (2005); B. Hou, J. Mei, M. Ke, W. Wen, Z. Liu, J. Shi, and P. Sheng, *ibid.* **76**, 054303 (2007).
[11] J. Christensen, A. I. Fernandez-Dominguez, F. de Leon-Perez, L. Martín-Moreno, and F. J. García-Vidal, Nat. Phys. **3**, 851 (2007); J. Christensen, L. Martín-Moreno, and F. J. García-Vidal, Phys. Rev. B **81**, 174104 (2010).
[12] Y. Zhou, M.-H. Lu, L. Feng, X. Ni, Y.-F. Chen, Y.-Y. Zhu, S.-N. Zhu, and N.-B. Ming, Phys. Rev. Lett. **104**, 164301 (2010).
[13] A. N. Norris and H. A. Luo, J. Acoust. Soc. Am. **82**, 213 (1987).
[14] R. C. McPhedran and D. Maystre, Appl. Phys. **14**, 1 (1977).
[15] F. J. García-Vidal, L. Martin-Moreno, T. W. Ebbesen, and L. Kuipers, Rev. Mod. Phys. **79**, 1267 (2007).

[16] B. Sturman, E. Podivilov, and M. Gorkunov, Phys. Rev. B **82**, 115419 (2010).
[17] I. A. Viktorov, *Rayleigh and Lamb Waves: Physical Theory and Applications* (Plenum, New York, 1967).
[18] V. M. García-Chocano, T. López-Rios, A. Krokhin, and J. Sánchez-Dehesa, AIP Adv. **1**, 041501 (2011).
[19] D. Achenbac, *Wave Propagation in Elastic Solids* (North-Holland, Amsterdam, 1973).
[20] N. E. Glass and A. A. Maradudin, J. Appl. Phys. **54**, 796 (1983).
[21] *Rayleigh-wave Theory and Applications*, edited by E. A. Ash and E. G. Paige (Springer-Verlag, New York, 1985).
[22] R. Sainidou and N. Stefanou, Phys. Rev. B **73**, 184301 (2006).
[23] H. Estrada, P. Candelas, A. Uris, F. Belmar, F. J. García de Abajo, and F. Meseguer, Phys. Rev. Lett. **101**, 084302 (2008).
[24] H. Estrada, F. J. García de Abajo, P. Candelas, A. Uris, F. Belmar, and F. Meseguer, Phys. Rev. Lett. **102**, 144301 (2009).
[25] P. P. Lloyd and M. Redwood, Acoustica **16**, 169 (1965).
[26] V. M. García-Chocano, Nagaraj, T. López-Rios, L. Gumen, J. Sánchez-Dehesa, and A. Krokhin, J. Acoust. Soc. Am. **132**, 2807 (2012).
[27] M. A. Seo, H. R. Park, S. M. Koo, D. J. Park, J. H. Kang, O. K. Suwal, S. S. Choi, P. C. M. Planken, G. S. Park, N. K. Park, Q. H. Park, and D. S. Kim, Nat. Photon. **3**, 152 (2009).
[28] X. Chen, H.-R. Park, N. C. Lindquist, J. Shaver, M. Pelton, and S.-H. Oh, Sci. Rep. **4**, 6722 (2014).
[29] R. H. Lyon, J. Acoust. Soc. Am. **27**, 259 (1955).
[30] Yu. I. Bobrovitskii, Akust. Zh. **18**, 513 (1972) [Sov. Phys.-Acoust. **18**, 432 (1973)].
[31] D. D. Zakharov, Comput. Math. Math. Phys. **50**, 1522 (2010).
[32] See Supplemental Material at http://link.aps.org/supplemental/10.1103/PhysRevB.91.094303 for the movie showing variation of pressure and displacements in the channel and in the plates during propagation of sound wave.